Excitation, relaxation, and quantum diffusion of CO on copper

Jean Christophe Tremblay,[*] Gernot Füchsel, and Peter Saalfrank

Institut für Chemie, Universität Potsdam, Karl-Liebknecht-Straße 24-25, D-14476 Potsdam-Golm, Germany
(Received 11 June 2012; revised manuscript received 7 July 2012; published 23 July 2012)

We investigate the effect of intermode coupling and anharmonicity on the excitation and relaxation dynamics of CO on Cu(100). The nonadiabatic coupling of the adsorbate to the surface is treated perturbatively using a position-dependent state-resolved transition rate model. Using the potential energy surface of Marquardt *et al.* [J. Chem. Phys. **132**, 074108 (2010)], which provides an accurate description of intermode interactions, we propose a four-dimensional model that represents simultaneously the diffusion and the desorption of the adsorbate. The system is driven by both rational and optimized infrared laser pulses to favor either selective mode and state excitations or lateral displacement along the diffusion coordinate. The dissipative dynamics is simulated using the reduced density matrix in its Lindblad form. We show that coupling between the degrees of freedom, mediated by the creation and annihilation of electron-hole pairs in the metal substrate, significantly affects the system excitation and relaxation dynamics. In particular, the angular degrees of freedom appear to play an important role in the energy redistribution among the molecule-surface vibrations. We also show that coherent excitation using simple IR pulses can achieve population transfer to a specific target to some extent but does not allow enforcement of the directionality to the diffusion motion.

PACS number(s): 68.43.Pq, 82.50.Bc, 32.80.Qk, 68.43.Jk

I. INTRODUCTION

The activation of adsorbate vibrations represents a major step in many reactions occurring at metallic surfaces, with potential application in molecule storage, nanoscale machines, and catalysis.[1–13] In particular, the diffusion motion plays a fundamental role in the latter process, where the reactive species move along the surface before meeting their reaction partner. The motion perpendicular to the surface is also important to describe, e.g., the release of adsorbates from the surface.[14–18] In some cases, the photoexcitation of selected modes using infrared laser pulses was shown to favor direct[19] and indirect adsorbate desorption.[16,18] State-selective vibrational excitation of adsorbed molecules was also proposed as a candidate for quantum computing, as well as a practical means of activating catalysts by loading the subsurface with reactive species.[20]

Our goal here is to perform infrared excitations of selected degrees of freedom in an adsorbate at a metal surface to eventually favor some reactions at the expense of others.[21–23] The diffusion and the hopping of the adsorbate, along with the angles describing its orientation, are of great interest here. Although their importance is still hotly debated for processes such as scattering or dissociative adsorption,[24–28] nonadiabatic effects are known to play a major role for reactions occurring when molecules remain close to metallic surfaces over an extended period of time.[5,13,29,30] In the strong-coupling limit, it is customary to use the independent electron surface hopping approach first proposed by Tully and co-workers.[31–36] In this case, classical molecular dynamics simulations are performed on a large number of potential energy surfaces used to represent the continuum of electronic states at the metal surface. The main issues are related to the evaluation of the coupling between electronic states and to the convergence of the discretized continuum. In the weak-coupling limit, fully quantum mechanical simulations can be performed, where all states of the continuum are included implicitly in a mean-field treatment of the nonadiabatic couplings.

Many perturbative expressions based on the electron self-energy,[29,37–39] time-dependent density functional theory[40,41], or electronic friction theory[25,42,43] were proposed over the years. To circumvent the limitations of these approaches, which rely on the local harmonic approximation, we developed a position-dependent, anharmonic transition rate model.[20,44] The derivation relates the electronic friction and self-energy approaches for the limiting case of a single atom in a harmonic well and was recently extended to treat polyatomic molecules.[19,45] For studying large-amplitude motions such as diffusion, anharmonicity, corrugation, and intermode coupling are bound to play an important role.

In the present paper, we focus our efforts on the vibrational control of CO on a Cu(100) surface. The system vibrational states were studied previously,[46–49] as were the associated lifetimes,[29,39] its dissipative dynamics,[50,51] and the selective excitation of desired states.[52,53] Most of the theoretical work was done using the potential energy surface of Tully and co-workers,[54] which was shown to describe the anharmonicity and intermode couplings of the adsorbate vibrations rather poorly.[46,47,50,53] These limitations were improved upon recently by Marquardt *et al.*,[55] who introduced a new global potential energy surface (PES) for diatomic molecules at surfaces that allows for more flexibility while retaining a sound physical interpretation for the fitting parameters. This PES was shown to well reproduce the diffusion barrier obtained from periodic density functional theory slab calculations, as well as other spectroscopic features of the system. In particular, anharmonic couplings are now much better described,[55] which prove to have a great influence on the selectivity of the coherent excitations investigated here.

The dissipative dynamics of the CO/Cu(100) system is studied using the reduced density matrix formalism, in which the effect of the environment, i.e., the creation and annihilation of electron-hole pairs in the metallic substrate, are treated implicitly. Because our simulations proceed on a picosecond time scale, we choose to neglect the short-term memory of

the surface and only instantaneous dissipation is included. We first investigate the relaxation dynamics of the system initially prepared in a pure state of a given mode. This gives insight into the strength of the intermode coupling in the system and the microscopic details of the relaxation mechanisms. Second, we perform IR-driven selective excitations from the global ground state of a CO molecule initially localized on top of a given copper atom. One aim is to tailor a laser pulse to excite the so-called surface mode, where the hopping of the molecule on the surface might convert into lateral motion and help overcome the diffusion barrier. This is done using rationally designed[56] as well as optimized pulses. The latter are obtained using locally optimal control theory,[57–66] where an objective functional designed to reach a desired target is optimized. Another goal is to activate directly the diffusion motion on the surface by using coherent excitations in an attempt to control the directionality of the motion.

In Sec. II, the vibrational wave functions of the CO/Cu(100) system are computed and analyzed. A numerical procedure for localizing the states of the adsorbate is introduced. In Sec. III, the reduced density matrix formalism and the perturbative model for describing electron-hole pair coupling are presented. The relaxation dynamics of chosen states is studied. In Sec. IV, a model global dipole moment surface is introduced and used to perform IR-driven excitations of selected targets. The conclusions are briefly summarized in the last section.

II. THE SYSTEM

A. Vibrational states

The full-dimensional Hamiltonian describing the adsorbate vibrations of a diatomic molecule can be written in orthogonal coordinates as

$$\hat{H} = -\frac{\hbar^2}{2m_s}\left(\frac{\partial^2}{\partial X^2} + \frac{\partial^2}{\partial Y^2} + \frac{\partial^2}{\partial Z^2}\right) - \frac{\hbar^2}{2\mu}\frac{\partial^2}{\partial r^2}$$
$$+ \frac{\hbar^2}{2\mu r^2}\hat{J}^2(\theta,\phi) + V(X,Y,Z,r,\theta,\phi), \quad (1)$$

where the angular momentum operator is given by[67]

$$\hat{J}^2(\theta,\phi) = -\left(\frac{\partial^2}{\partial\theta^2} + \cot(\theta)\frac{\partial}{\partial\theta} + \frac{1}{\sin^2(\theta)}\frac{\partial^2}{\partial\phi^2}\right). \quad (2)$$

The coordinates $\{X,Y,Z\}$ describe the position of its center of mass and $\{r,\theta,\phi\}$ its shape and orientation, as depicted in Fig. 1, and m_s and μ are the total and reduced mass of the adsorbate, respectively. The surface is assumed to be rigid. For CO on Cu(100) an accurate, global potential energy surface $V(X,Y,Z,r,\theta,\phi)$ based on the Strasbourg-Amsterdam-Potsdam (SAP) fitting scheme is readily available.[55]

The diffusion process which we investigate here implies very large amplitude motion in the plane parallel to the surface. This renders the calculations tedious and even impracticable for studying wave packets evolving over multiple unit cells on the surface. We advocate using a reduced-dimensional model that captures the physics of the process. By exploiting the symmetry of the surface, the diffusion is studied along the X axis and the Y coordinate is kept frozen at its equilibrium value. Since the r coordinate presents a much higher vibrational frequency than all other modes (see Table I), it can therefore be
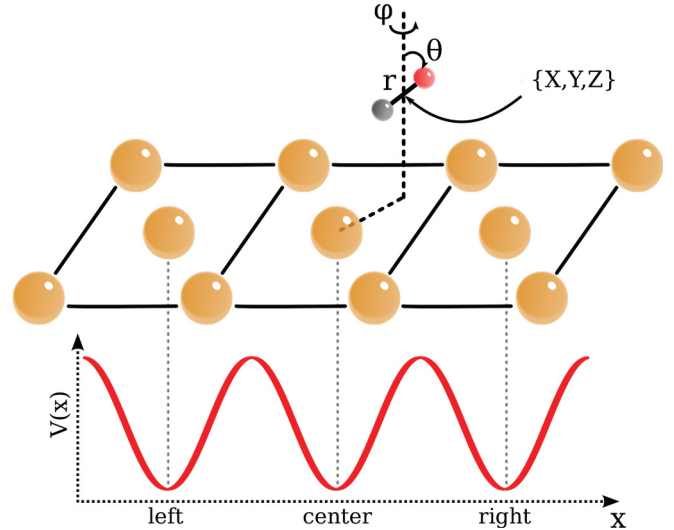

FIG. 1. (Color online) Definition of the coordinates for the CO on Cu(100) system. Only the copper atoms of the first layer are represented. A cartoon of the 1D PES along the X axis bisecting the central copper atoms of three adjacent unit cells is depicted in the lower panel.

considered adiabatically separable and is neglected here (i.e., $r = r_0$), yielding an effective four-dimensional (4D) model

$$\hat{H}_{4D} = -\frac{\hbar^2}{2m_s}\left(\frac{\partial^2}{\partial X^2} + \frac{\partial^2}{\partial Z^2}\right) + \frac{\hbar^2}{2\mu r_0^2}\hat{J}^2(\theta,\phi)$$
$$+ V(X,Z,\theta,\phi;Y_0;r_0). \quad (3)$$

The vibrational states of the adsorbate are computed by solving the time-independent Schrödinger equation, $\hat{H}_{4D}\psi_n = E_n\psi_n$, in a tensor product of one-dimensional (1D) discrete variable representation (DVR) functions[68–77]

$$\psi_n = \sum_{i_x,i_z,i_\theta,i_\phi} C^{(n)}_{i_x,i_z,i_\theta,i_\phi}\varphi_{i_x}(X)\varphi_{i_z}(Z)\varphi_{i_\theta}(\theta)\varphi_{i_\phi}(\phi), \quad (4)$$

where $\varphi_j(q_j)$ is the jth basis function for mode q_j. The X coordinate is represented using 111 plane-wave DVR points[69] on the range $[-3.8181,3.8181]$ Å, covering three unit cells. This will allow us to study the directionality of the diffusion process. The Z basis is composed of 25 potential optimized DVR functions[72,73] contracted from 100 sinc-DVR functions[71] on the range $[1.5875,3.1751]$ Å for a 1D reference potential obtained by freezing all remaining coordinates to their equilibrium value ($X = Y = \theta = \phi = 0$ and $r = 1.154$ Å). For the azimuthal angle, a basis of 25 Gauss-Chebyshev-DVR functions on the range $]0,2\pi[$ is used. Finally, 17 Gauss-Legendre-DVR points on the range $]0,\pi/6[$

TABLE I. Comparison of the vibrational transition energies (in hc/cm) with the experimental and literature values.

Assignment	4D model	Marquardt	Experiment
T mode	10.9	16.5	31.8
R mode	288.0	288.0	285.0
S mode	307.8	300.6	345.0
CO stretch	–	2052.9	2079.0

obtained from the contraction of 101 Legendre functions are used to represent angle θ, avoiding the singularity at $\theta = 0$.

The lowest lying eigenstates of the resulting matrix are extracted using a coupled two-term Lanczos eigensolver with full reorthogonalization, which allows us to recover the true degeneracy of the vibrational states.[17,53,78] In order to favor convergence at low energies, an inexact spectral transform was used to stretch the desired part of the spectrum and contract the undesired one. The idea is reminiscent of the MINRES filter diagonalization method of Yu and co-workers[79,80] and of the preconditioned inexact spectral transform approach of Huang and Carrington,[81–83] where a Lanczos subspace is built from the operation of a *function* of the Hamiltonian on a random starting vector. Specifically, we generate an orthogonal Krylov subspace using the function

$$f(\hat{H}_{4D}) = \tanh(a\hat{H}_{4D}) \simeq \sum_{k=0}^{n} C_k T_k\left(\cos\left(\frac{\hat{H}_{4D} - h_c}{\Delta H}\right)\right), \tag{5}$$

where $a = 10^{-3}E_h$ defines the steepness of the spectral transform, $h_c = 250500\ hc/cm$ is the midpoint of the Hamiltonian spectrum, and $\Delta H = 250\,100\ hc/cm$ its norm. As in Ref. 80 the coefficients C_k are obtained from the approximate expansion of the function using a discrete number $n = 20$ of Chebyshev polynomials $T_k[k\cos(x)]$. The eigenvectors associated with eigenvalues below a user-defined physical threshold are then assembled and used to compute the expectation value of the Hamiltonian operator. This method accelerates considerably the convergence of the targeted eigenvalues. From a set of 5000 orthogonalized Lanczos vectors, we recover 1318 eigenfunctions with energy below $1700\ hc/cm$. By analyzing the nodal structure within a single unit cell, we can assign the vibrational eigenstates to the different modes.

Table I shows the comparison of the reduced dimension model with the six-dimensional (6D) reference value of Marquardt *et al.*[55] as well as with the experiments.[84–86] The T, R, and S mode labels refer to the frustrated translations $\{X,Y\}$, the frustrated rotations $\{\theta,\phi\}$, and the surface mode Z. The frequencies are in good agreement with that of the full-dimensional calculation, although the T mode is slightly too low, in particular in comparison to the experiment. These discrepancies are partially due to the limitation of the potential itself and to the neglect of residual coupling with the frozen Y and r coordinates. These disparities should only have a modest influence on the qualitative behavior of the dynamical simulations reported in the present paper.

B. Localization procedure

The wave functions extracted from the Hamiltonian matrix are mostly delocalized above the three unit cells spanned by the basis. Diffusion is intrinsically a local process, where an initially localized wave function spreads sequentially to the neighboring unit cells. Within this physical picture, it is necessary to localize the vibrational eigenfunctions obtained from the Lanczos diagonalization. Since we study the dynamics in three unit cells along the X axis, we choose to take three functions within a small energy window ($\Delta E = \pm 20\ hc/cm$)

and localize them in either the left, central, or right well (see Fig. 1). The localization is done numerically as follows:

(1) For a given eigenstate α from the list of Lanczos eigenvalues, select two partners α_1 and α_2 within the energy window to form a triplet.

(2) Build and diagonalize the 3×3 matrix of overlaps in the central region:

$$\mathbf{S}_c^{(\alpha)}\mathbf{U}_c^{(\alpha)} = \mathbf{U}_c^{(\alpha)}\sigma_c^{(\alpha)}, \quad S_{c,ij}^{(\alpha)} = \int_{\text{center}} \psi_i^* \psi_j d\tau.$$

(3) Transform the three vectors to the temporary basis:

$$(\tilde{\psi}_1\ \tilde{\psi}_2\ \tilde{\psi}_c) = \mathbf{U}_c^{(\alpha)^t}(\psi_\alpha\ \psi_{\alpha_1}\ \psi_{\alpha_2}).$$

(4) Build and diagonalize the 2×2 matrix of the overlaps in the left region for the two delocalized vectors $\tilde{\psi}_1$ and $\tilde{\psi}_2$:

$$\mathbf{S}_l^{(\alpha)}\mathbf{U}_l^{(\alpha)} = \mathbf{U}_l^{(\alpha)}\sigma_l^{(\alpha)}, \quad S_{l,ij}^{(\alpha)} = \int_{\text{left}} \tilde{\psi}_i^* \tilde{\psi}_j d\tau.$$

This yields simultaneously the left and right localized vectors. The nodal structure of the localized functions should be further checked by computing their overlap in the left region after translating the right wave function to the left region.

(5) Form the proper unitary transformation matrix:

$$\mathbf{U}^{(\alpha)} = \mathbf{U}_c^{(\alpha)}\begin{pmatrix} \mathbf{U}_l^{(\alpha)} & 0 \\ 0 & 1 \end{pmatrix}.$$

(6) Transform the three vectors $\{\psi_\alpha, \psi_{\alpha_1}, \psi_{\alpha_2}\}$ to the localized basis:

$$(\psi_l^{(\text{loc})}\ \psi_r^{(\text{loc})}\ \psi_c^{(\text{loc})}) = \mathbf{U}^{(\alpha)^t}(\psi_\alpha\ \psi_{\alpha_1}\ \psi_{\alpha_2}).$$

(7) Cycle steps 1–6 for all possible partners α_1 and α_2 within the energy window to find the triplet that maximizes the overlaps:

$$s_l = \int_{\text{left}} \psi_l^{(\text{loc})^*}\psi_l^{(\text{loc})}d\tau, s_c = \int_{\text{center}} \psi_c^{(\text{loc})^*}\psi_c^{(\text{loc})}d\tau, \quad \text{and}$$

$$s_r = \int_{\text{right}} \psi_r^{(\text{loc})^*}\psi_r^{(\text{loc})}d\tau.$$

The procedure is repeated for another α eigenstate until all eigenstates have been transformed. From the $\mathbf{U}^{(\alpha)}$, we can build a unitary block matrix to toggle from the localized to the delocalized basis:

$$\mathbf{U} = \mathbf{U}^{(1)} \otimes \mathbf{U}^{(2)} \otimes \ldots \otimes \mathbf{U}^{(\alpha)} \otimes \ldots \otimes \mathbf{U}^{(n_t)}, \tag{6}$$

where n_t is the number of triplets. The operators can be simply transformed from the delocalized representation to the localized picture:

$$\hat{H}_{\text{loc}} = \mathbf{U}^t \hat{H}_{4D} \mathbf{U}. \tag{7}$$

From the 1318 eigenvalues extracted from the Lanczos run, 329 triplets were deemed localizable, i.e., more than 50% of the wave functions are found in the respective well. The remaining ~ 300 functions are located at the top of the calculated spectrum at energies much higher than the diffusion barrier, and they were discarded from the basis for the dynamics. The translation operator was applied to the resulting functions to confirm that the same nodal structure is found in each well. The results of the localization procedure are shown in Fig. 2, for example, for a highly excited state of the T mode. The
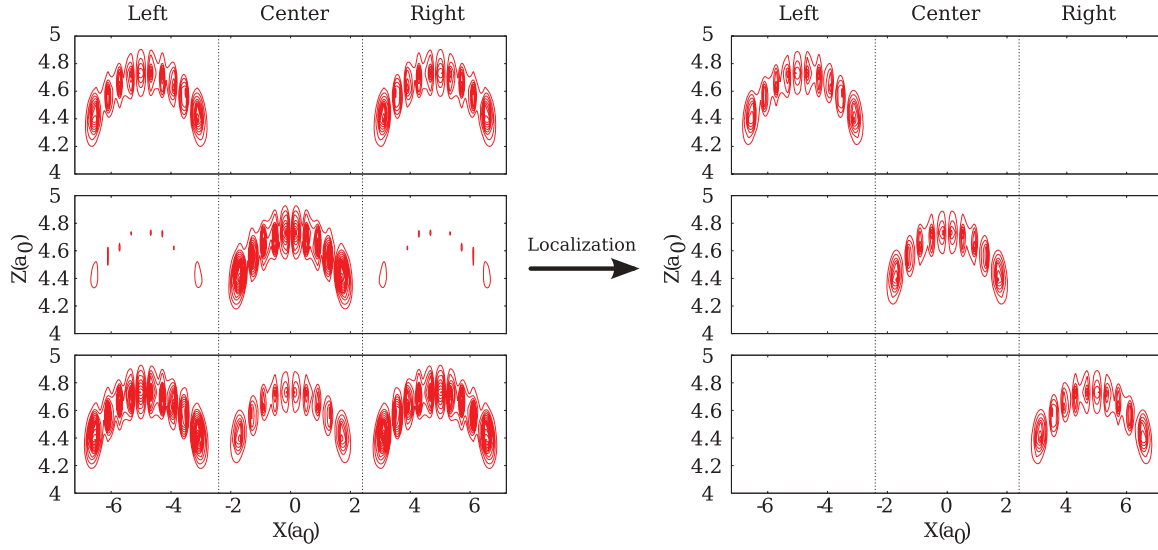
FIG. 2. (Color online) Probability density of the 9th excited state of the T mode before localization (left panels) and after localization (right panels). The 2D profiles are obtained by integrating all remaining coordinates. The dotted lines mark the separation between unit cells.

quantum number refers to the number of nodes along the X coordinate in a single unit cell. On the left, the wave functions as obtained from the Lanczos diagonalization are shown. After the localization procedure, the amplitude in the other wells is negligible. All triplet wave functions were inspected individually to ensure an appropriate localization. Higher excited states are more delocalized among the three wells but remain mostly localized on top of a single copper atom. The shortest tunneling time allowed in the present localized basis is about $\tau_{\text{tunnel}} \simeq \frac{\hbar\pi}{20 \text{ cm}^{-1}} \simeq 0.8$ ps. Note that all low-lying states are perfectly localized so that, consequently, the tunneling rates numerically vanish. To simplify later discussions, a compact notation for the vibrational eigenstates is introduced. The label $|\nu_X, \nu_Z, \nu_\theta, \nu_\phi; i\rangle$ represents the vibrational state located in the ith well ($i = \{l, c, r\}$ for the left, center, and right localized states) with ν_j quanta along coordinate q_j.

III. DISSIPATIVE DYNAMICS

A. Reduced density matrix

The contact of the adsorbate with the surface can lead to the creation and annihilation of electron-hole pairs in the metallic substrate and ultimately to energy exchange in the system. To study the dissipative dynamics of the adsorbate we advocate using the reduced density matrix formalism. The system temporal evolution is described by the Liouville–von Neumann equation

$$\dot{\hat{\rho}}(t) = -\frac{i}{\hbar}[\hat{H}, \hat{\rho}(t)] + \frac{i}{\hbar}\sum_q F_q(t)[\hat{\mu}_q, \hat{\rho}(t)] + \mathcal{L}_D\hat{\rho}, \quad (8)$$

where $\hat{\rho}(t)$ is the reduced density matrix operator, $F_q(t)$ is an external electric field polarized along the q axis, $\hat{\mu}_q$ is the qth component of the dipole moment operator, and $\mathcal{L}_D$ is the dissipative superoperator characterizing the interaction of the adsorbate with its environment. Neglecting memory effects in the substrate, which is appropriate considering that electron-hole pairs have a lifetime on the order of the femtosecond in

metallic environments, we can write the dissipative term in the Lindblad form[87]

$$\mathcal{L}_D = \sum_k \frac{1}{2}([\hat{C}_k, \hat{\rho}(t)\hat{C}_k^\dagger] + [\hat{C}_k\hat{\rho}(t), \hat{C}_k^\dagger]), \quad (9)$$

where the operator $\hat{C}_k$ represents the kth dissipative channel. In the basis of the localized eigenfunctions, the equations of motion in the interaction picture have a particularly compact appearance, here given in matrix notation:

$$\frac{d}{dt}\underline{\underline{\rho}}^{(I)}(t) = e^{i\underline{\underline{H}}^{(\text{loc})}t/\hbar} \cdot \left\{ \frac{i}{\hbar}\sum_q F_q(t)[\underline{\underline{\mu}}^{(q)}, \underline{\underline{\rho}}^{(s)}(t)] \right.$$
$$+ \sum_k \underline{\underline{C}}_k\underline{\underline{\rho}}^{(s)}(t)\underline{\underline{C}}_k^\dagger - \sum_k \frac{1}{2}(\underline{\underline{C}}_k^\dagger\underline{\underline{C}}_k\underline{\underline{\rho}}^{(s)}(t)$$
$$\left. + \underline{\underline{\rho}}^{(s)}(t)\underline{\underline{C}}_k^\dagger\underline{\underline{C}}_k \right\} \cdot e^{-i\underline{\underline{H}}^{(\text{loc})}t/\hbar}, \quad (10)$$

with $e^{\pm i\underline{\underline{H}}^{(\text{loc})}T/\hbar} = \underline{\underline{U}}e^{\pm i\underline{\underline{E}}^{(\text{deloc})}t/\hbar}\underline{\underline{U}}^t$. The matrices $\underline{\underline{\mu}}^{(q)}$ contain the transition dipole elements. The superscripts (I) and (s) refer to the interaction and Schrödinger picture, respectively. Due to the sparsity of the $\underline{\underline{C}}_k$ matrices, the reduced density matrix propagation scales formally as N_b^3 for a basis of size N_b. The equations of motion can be efficiently propagated using a preconditioned Runge-Kutta integrator.[65,88,89]

B. Relaxation process

The dissipation due to the adsorbate coupling to the surface will mainly lead to energy relaxation in the system. This can be characterized by the Lindblad operators

$$\hat{C}_k \rightarrow \hat{C}_{m\rightarrow n} = \gamma_{m\rightarrow n}^{1/2}|n\rangle\langle m|, \quad (11)$$

which transfer the population from state $|m\rangle$ to state $|n\rangle$ at a rate $\gamma_{m\rightarrow n}$. The dominating contribution to the energy relaxation rates in adsorbate-metal systems is the creation of electron-hole pairs in the metal. In the weak-coupling limit,

TABLE II. Inverse of the state-to-state transition rates (lower triangle, in picoseconds) and transition dipole elements along z (upper triangle, in ea_0) for selected 4D vibrational states of the central unit cell. The transition energies are reported in the last column. The zero-point energy is located at 457.11 hc/cm.

Label	$|0,0,0,0;c\rangle$	$|1,0,0,0;c\rangle$	$|2,0,0,0;c\rangle$	$|3,0,0,0;c\rangle$	$|0,0,0,1;c\rangle$	$|0,1,0,0;c\rangle$	$|0,0,1,0;c\rangle$	Energy
$|0,0,0,0;c\rangle$	...	$\sim 10^{-9}$	0.04603	$\sim 10^{-10}$	$\sim 10^{-10}$	0.01506	0.00128	0.0
$|1,0,0,0;c\rangle$	108	...	$\sim 10^{-9}$	0.06592	0.00273	$\sim 10^{-9}$	$\sim 10^{-8}$	10.9
$|2,0,0,0;c\rangle$	34.6	42.7	...	$\sim 10^{-9}$	$\sim 10^{-10}$	0.00247	0.00057	24.7
$|3,0,0,0;c\rangle$	3790	22.9	25.9	...	0.00072	$\sim 10^{-11}$	$\sim 10^{-8}$	39.9
$|0,0,0,1;c\rangle$	132	2.30	$\sim 10^{6}$	$\sim 10^{4}$	...	$\sim 10^{-8}$	$\sim 10^{-8}$	288.0
$|0,1,0,0;c\rangle$	82.0	237	71.0	$\sim 10^{4}$	169	...	0.00248	307.8
$|0,0,1,0;c\rangle$	0.862	$\sim 10^{6}$	61.9	$\sim 10^{7}$	147	92.0	...	568.7

this can be treated perturbatively using Fermi's golden rule, where the coupling is mediated by the kinetic energy operator of the adsorbate nuclei. We derived recently a rate expression based on electronic friction theory that takes into account the anharmonicity of the vibrational wave functions, as well as the surface corrugation:

$$\gamma_{m \to n} = \sum_q \gamma^{(q)} \left| \langle n | \rho_{embd}^{1/3} \frac{\partial}{\partial q} | m \rangle \right|^2. \quad (12)$$

The embedding density ρ_{embd} is the electronic density surrounding the adsorbate and it describes approximately the position dependence of the nonadiabatic couplings in the vicinity of the surface. The integrals are performed over all coordinates to include intermode coupling. The constants are chosen to reproduce the state-to-state transition rates of a set of reference states obtained by *ab initio* calculations for a given frozen geometry.[29,54] Here, the embedding density is obtained by performing a periodic density functional theory calculation for the bare copper surface using the PW91 functional,[90] as implemented in VASP.[91,92] The total energy of a slab containing six copper layers for the 1×1 unit cell is minimized while relaxing the position of all atoms. The plane-wave basis used for the calculation is defined by an energy cutoff of 273.246 eV and a $15 \times 15 \times 15$ Monkhorst-Pack grid is used for the k-point sampling.[93]

The X- and Z-mode contributions are scaled so that the inverse transition rates associated with the $|1,0,0,0;c\rangle \to |0,0,0,0;c\rangle$ and $|0,1,0,0;c\rangle \to |0,0,0,0;c\rangle$ transitions reproduce the first-principles lifetimes of 108 and 82 ps, respectively ($\gamma^{(X)} = 3.3204 \times 10^{-6} E_h a_0^4/\hbar$ and $\gamma^{(Z)} = 1.3047 \times 10^{-7} E_h a_0^4/\hbar$).[29] Upon inspection of the integrals $\langle n | \rho_{embd}^{1/3} \frac{d}{d\theta} | m \rangle$ and $\langle n | \rho_{embd}^{1/3} \frac{d}{d\phi} | m \rangle$, it became clear that the ϕ coordinate does not play an important role in the relaxation process since the latter matrix elements are almost zero for all transitions. Hence, the constant $\gamma^{(\phi)}$ is set to zero to avoid numerical problems upon scaling; i.e., the decay mediated by ϕ can be neglected altogether. Further, the relaxation from the first ϕ-mode excited state does not appear to decay to the global ground state, with $\langle 0,0,0,1;c | \rho_{embd}^{1/3} \frac{d}{d\theta} | 0,0,0,0;c \rangle \simeq 0$. Hence, we scale the decay rate of the R mode to the reference value[29,54] of 2.3 ps using the largest contribution to its relaxation, namely the intermode transition to the first X-excited state mediated by the θ coordinate ($\gamma^{(\theta)} = 2.5268 \times 10^{-6} E_h a_0^4/\hbar$). The relaxation times ($\tau_{m \to n} = 1/\Gamma_{m \to n}$) for selected vibrational

states in the central unit cell can be seen in the lower left entries of Table II. Intermode coupling plays an important role already at those low frequencies. For example, the S mode decays as efficiently to the ground state as to the second excited state of the T mode. Similar observations can be made for the R mode, where the first ϕ excited state decays preferentially to the T mode.

These trends are confirmed by looking at the population dynamics of selected excited states, as reported in Fig. 3. In the top right panel, we can see that the energy stored along the ϕ coordinate preferentially decays to the T mode; i.e., it transfers a large part of its population to the translational coordinate. As discussed above, this transfer is mediated mainly by the gradient along θ. The ground state remains only marginally populated on this time scale. This is not the case for lower right panel, where the energy is stored in the first θ state of the R mode. Within about 800 fs, the population reverts almost quantitatively to the ground state, with residual population found mostly in the second excited state of the T mode. Because the initial θ state, the final T-mode state, the gradient along θ, and the embedding density ρ_{embd} are all totally symmetric around the minimal geometry, it is not surprising to see that transitions to odd states (e.g., $|1,0,0,0;c\rangle$)
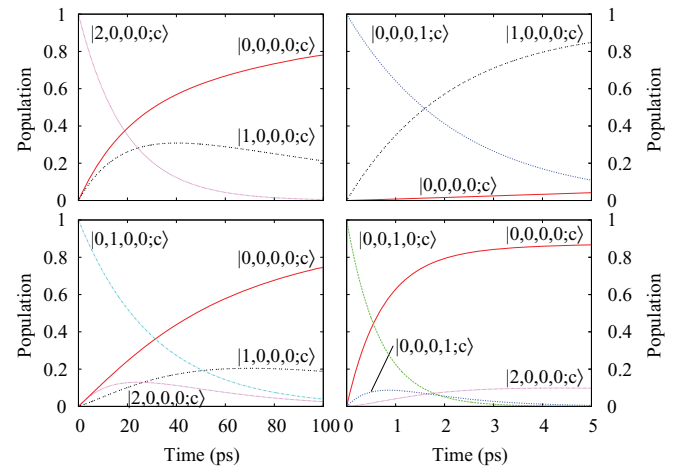

FIG. 3. (Color online) Relaxation dynamics of selected eigenstates of CO on Cu(100) located in a single unit cell. The initial states belong to the T mode ($|2,0,0,0;c\rangle$, top left panel), the S mode ($|0,1,0,0;c\rangle$, bottom left panel), and the R mode ($|0,0,0,1;c\rangle$ and $|0,0,1,0;c\rangle$ in the top and bottom right panels, respectively).
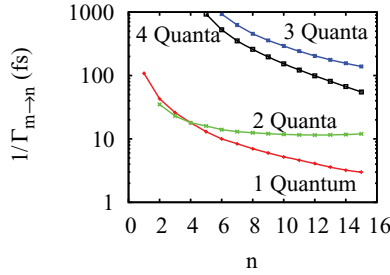
FIG. 4. (Color online) Contribution of the different dissipative channels for the energy relaxation of highly excited states of the T mode. The quantum number m refers to the initial state, $|m,0,0,0;c\rangle$. The inverse transition rates $(1/\Gamma_{m\to n})$ for the relaxation from state $|m,0,0,0;c\rangle$ to state $|n,0,0,0;c\rangle$ are depicted in red ($m-n=1$ quantum), green ($m-n=2$ quanta), blue ($m-n=3$ quanta), and black ($m-n=4$ quanta), respectively.

are suppressed. In the lower left panel it can be seen that the S mode also efficiently transfers population to the T mode, again following the symmetry prescriptions described above.

An important finding is that multiple quanta relaxation is possible due to inclusion of the wave function anharmonicity, as evidenced from the relatively fast rates of the $|3,0,0,0;c\rangle \to |1,0,0,0;c\rangle$ and $|2,0,0,0;c\rangle \to |0,0,0,0;c\rangle$ transitions in Table II. This appears also in the relaxation dynamics of the second excited state of the T mode in the top left panel of Fig. 3, where the direct relaxation to the ground state provides competition for the sequential relaxation. As can be seen from Fig. 4, this trend is confirmed for higher excited states. As the number of quanta along the T mode increases, other dissipative channels, such as the three-quanta and four-quanta relaxation mechanisms, also become competitive. Also, for low quantum numbers, the even-quanta relaxation mechanisms seem to play a dominant role. This is probably due to the wave functions' symmetry, whereas with the increasing delocalization of the higher excited states, the overlap between energetically separated states dwindle and with them the associated transition probabilities [see Eq. (12)].

A final word must be made concerning the relaxation *between* potential wells. At the low energies reported above, the relaxation remains localized in a single potential well. For states with energies above and close to the top of the diffusion barrier ($\Delta E^{\ddagger} \sim 500\ hc/$cm), coupling between states localized in different wells is indeed possible. The usual approach to calculate relaxation rate of multiwell problems relies on a simple truncated, local harmonic approximation. This prohibits relaxation between potential wells. In our formalism, the extension from a single to multiple potential wells is straightforward, since the integrals in Eq. (12) are computed numerically exactly. The effect can be seen in Fig. 5, where the relaxation dynamics of a highly excited state of the central well is depicted. The complex nodal structure of the probability density in the XZ plane of the initial state, for which a clear assignment remains elusive, is shown in the inset. The populations of states localized in the left, central, and right wells are summed and plotted in green, black, and blue, respectively. Upon relaxation, most of the population remains in the central well, with about 20% falling in either of the other minima. The small population discrepancy between
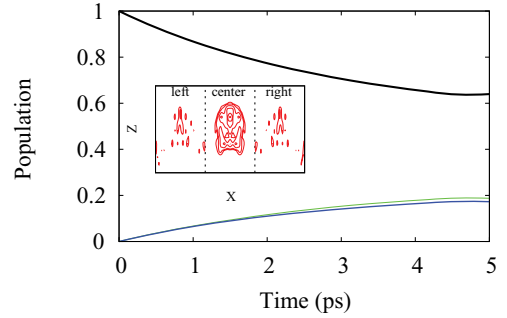

FIG. 5. (Color online) Relaxation of a highly excited central state. The 2D density in the XZ plane of the initial state is shown in the inset. The sum of population of states localized in the left, central, and right wells are shown in green, black, and blue, respectively.

the left and right wells can be traced back to the imperfect numerical localization procedure. Provided that the population of an initially localized adsorbate can reach a state close to the diffusion barrier, lateral diffusion should be possible.

IV. IR-DRIVEN EXCITATIONS

A. Dipole moment

To steer the adsorbate dynamics we use short and intense laser pulses. The oscillating electric fields are treated in the semiclassical dipole approximation, as shown in Eq. (8). A global dipole moment surface (DMS) is required to evaluate the transition dipole elements in Eq. (10). The 4D function available from the literature[53] only treats the z component of $\hat{\mu}$ along the r, Z, θ, and ϕ coordinates of the adsorbate; i.e.. the dependency along the diffusion direction is neglected. To circumvent this limitation, we propose a new model dipole surface obtained from density functional theory (DFT) calculations on small copper clusters. The CO adsorbate is here treated as a classical dipole with orientation $\{\theta,\phi\}$, yielding a dipole moment vector

$$\vec{\mu}(X,Z,\theta,\phi) = \begin{pmatrix} \mu_z(X,Z) & \sin(\theta) & \cos(\phi) \\ \mu_z(X,Z) & \sin(\theta) & \sin(\phi) \\ \mu_z(X,Z) & \cos(\theta) \end{pmatrix}. \quad (13)$$

The z dependence of the two-dimensional (2D) dipole moment $\mu_z(X,Z)$ can be simplified by exploiting the periodicity of the surface:

$$\mu_z(X,Z) = \mu_{\text{top}}(Z) \cos^2\left(\frac{\pi X}{L}\right) + \mu_{\text{brg}}(Z) \sin^2\left(\frac{\pi X}{L}\right), \quad (14)$$

where L is the distance between two copper atoms along the x direction, and the $\mu_i(Z)$ describe the Z dependence of the dipole moment along the space-fixed z axis for a CO molecule sitting perpendicularly on top of a copper atom (labeled top) or between two copper atoms (labeled brg) of the surface. The trigonometric functions switch the dipole moment from one symmetric site to the other smoothly along the X axis. The corrugation of the surface is thus properly included while its anisotropy, which does not play an important role in the present case, is neglected.
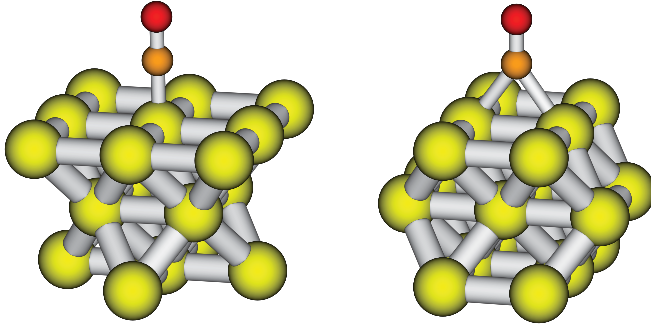
FIG. 6. (Color online) Structure of Cu_{18} clusters used to compute the dipole moment of CO adsorbed on top (left) and at the bridge site (right) of a Cu(100) surface. The yellow, orange, and red balls represent copper, carbon, and oxygen atoms, respectively.

The two 1D dipole functions are obtained by fitting DFT calculations to Cu_{18} clusters that have the symmetry at the sites of interest. Specifically, three-layer clusters with 9-4-5 and 6-6-6 arrangements were used to represent the copper surface at the top and bridge sites, respectively (see Fig. 6).

The z component of the dipole moment for different Z positions of the adsorbate are computed using the CAM-B3LYP functional,[94] as implemented in the GAUSSIAN09 program package.[95] The LANL2 effective core potential (ECP) and the associated triple-zeta basis are used for all copper atoms,[96–98] and Dunning's cc-pVTZ bases were used for the adsorbate atoms.[99] Both curves are fitted to asymmetric Eckart barriers:

$$\mu_i(Z) = \mu_{i,0} + a_{i,1} \left(\frac{e^{-(Z-\zeta_i)/b_i}}{(1 + e^{-(Z-\zeta_i)/b_i})} \right)$$
$$+ a_{i,2} \left(\frac{e^{-(Z-\zeta_i)/b_i}}{(1 + e^{-(Z-\zeta_i)/b_i})^2} \right). \quad (15)$$

The fit parameters are reported in Table III. The asymptotic values are then adjusted to the dipole moment of a free-standing CO molecule ($\mu_{i,0} = \mu_{CO}^{(gas)} = 0.0365ea_0$).

The transition dipole moments along the z direction, $\mu_{mn}^{(z)} = \langle m|\mu_z(X,Z)\cos(\theta)|n\rangle$, between selected states $|m\rangle$ and $|n\rangle$ are shown in the upper right part of Table II. It can be seen that excitation of the S mode ($|0,0,0,0;c\rangle \rightarrow |0,1,0,0;c\rangle$, $\mu_{mn} = 0.01506ea_0$) is about an order of magnitude larger than for the θ mode ($|0,0,0,0;c\rangle \rightarrow |0,0,1,0;c\rangle$, $\mu_{mn} = 0.00128ea_0$) and that ϕ-mode excitations ($|0,0,0,0;c\rangle \rightarrow |0,0,0,1;c\rangle$, $\mu_{mn} \sim 10^{-10}ea_0$) are forbidden. This is consistent with the trends observed for the transition dipoles obtained using the reference function from the literature.[53,100] In the later case, the absolute

TABLE III. Fit parameters for the z component of the dipole moment for CO on Cu(100) along the Z coordinate.

Parameter	Top	Bridge
$\mu_{i,0}$	$-0.0478ea_0$	$-0.006173ea_0$
$a_{i,1}$	$-0.09305ea_0$	$-0.3343ea_0$
$a_{i,2}$	$1.0465ea_0$	$0.1966ea_0$
b_i	$0.4584a_0$	$0.0718a_0$
ζ_i	$4.9141a_0$	$4.8154a_0$
$\mu_{CO}^{(gas)}$	$0.0365ea_0$	$0.0365ea_0$

value of the transition dipole moments are about 2–3 times larger, indicating that the slope of the DMS close to equilibrium is larger. These discrepancies can be traced back to the model used to compute the dipole function. Whereas we use small core ECPs for all 18 copper atoms in our clusters, an unbalanced description was chosen by Ricart *et al.*[100] There, a large-core ECP and a minimal basis were used to describe the four atoms forming the bottom layer of a pyramidal Cu_5 cluster. The top layer was formed of a single copper atom described by a small-core ECP and a larger basis, on which the CO molecule was adsorbed. The cluster itself thus has a very large permanent dipole and is also inadequate for representing adsorption on a bridge site (i.e., between two copper atoms). We compared our results with perturbative MP2 calculations, as well as with coupled cluster references. Curves similar to those for the DFT/CAM-B3LYP case were observed for the Z dependence of the dipole moment for the top position. We thus believe that the approach followed here yields a physically more accurate description of the dipole moment surface.

It is interesting to note that, although the fundamental excitation of the T mode is forbidden by symmetry, the totally symmetric first overtone is relatively easy to excite using a z-polarized field ($|0,0,0,0;c\rangle \rightarrow |2,0,0,0;c\rangle$, $\mu_{mn} = 0.04603ea_0$). This is also the case for all two-quanta transitions ($|1,0,0,0;c\rangle \rightarrow |3,0,0,0;c\rangle$, $|2,0,0,0;c\rangle \rightarrow |4,0,0,0;c\rangle$, etc.). This is due to the relatively large x dependence of the dipole moment, which can be traced back to the strong coupling of the wave functions in the XZ plane (see Fig. 2). Further, as was discussed previously elsewhere, the carbon atom ventures much closer to the surface at the bridge stationary point (2.212 Å versus 2.499 Å for the top position). In the simple Blyholder picture, the increased back donation to the antibonding orbitals of the adsorbate weakens the CO bond r, whose length increases from 1.154 to 1.174 Å. Hence, the dipole moment at the bridge position is bound to be larger than at the top position, and with it the z dependency of the dipole moment.

Finally, it must be noted that, although it is not possible to excite the angular ϕ mode using a z-polarized field, the excitation can be performed efficiently using an x-polarized field. This is due to the relatively large transition dipole moment along the x direction, $\mu_{mn}^{(x)} = 0.01506ea_0$, which is otherwise vanishingly small along the z direction. Another interesting point is that, although the first excited state of the T mode is also strongly coupled to the ground state via the x component of the dipole ($\mu_{mn}^{(x)} = 0.01034ea_0$), the transition to higher excited states is less efficient ($\mu_{mn} \sim 0.0060107ea_0$ for $|1,0,0,0;c\rangle \rightarrow |2,0,0,0;c\rangle$, $\mu_{mn} \sim 0.001573ea_0$ for $|2,0,0,0;c\rangle \rightarrow |3,0,0,0;c\rangle$, etc.). This is a sign of great anharmonicity, which renders vibrational ladder climbing inefficient and proves eventually futile for favoring lateral motion of the adsorbate.

B. Mode selectivity and quantum diffusion

Using the model DMS and the 4D eigenfunctions obtained above, we first perform infrared excitations of selected modes of the adsorbed CO in order to evaluate the controllability of the system. Since our ultimate goal is to study the directionality of the diffusion process, we start our simulations from the ground state of the central well. We perform excitations of states that have relatively large transition dipole moments

and that can potentially be used to induce a lateral displacement. These include the direct excitation of the T-mode overtones, $|0,0,0,0;c\rangle \rightarrow |2,0,0,0;c\rangle \rightarrow |4,0,0,0;c\rangle \rightarrow \ldots$, the indirect excitation of the θ coordinate via the ϕ mode, $|0,0,0,0;c\rangle \rightarrow |0,0,0,1;c\rangle \rightarrow |0,0,1,0;c\rangle$, and vibrational ladder climbing along the S mode, $|0,0,0,0;c\rangle \rightarrow |0,1,0,0;c\rangle \rightarrow |0,2,0,0;c\rangle \rightarrow |0,3,0,0;c\rangle$. The latter assignments are a bit loose since intermode coupling is very strong already for the second S-mode excited state, and the nodal structure is thus more difficult to determine unambiguously.

The adsorbate is excited using q-polarized π pulses of the form

$$F_q(t) = F_{0,q} \, \sin^2\left(\frac{\pi t}{\Delta T}\right) \cos(\omega t), \qquad (16)$$

which are tailored to completely invert the population in an isolated two-level system. For a pulse of duration ΔT, the field amplitude for the transition from state $|m\rangle$ to state $|n\rangle$ is given analytically by $F_{0,q} = \frac{2\hbar\pi}{|\mu_{mn}^{(q)}|\Delta T}$. The population dynamics driven by z-polarized π pulses tuned at the S-mode transition frequency can be seen from the top panel of Fig. 7, along with the sum of the depicted states. Most of the population ($\sim 75\%$) is found in the states shown in the figure at the end of the pulse, with the dominating contribution coming from the fundamental ($\sim 30\%$). Note that the combination band $|0,1,0,1;c\rangle$ is also significantly populated—an example of intermode coupling. The remaining population is found in the higher harmonics of the S mode but remain centered in the central well, although already well above the diffusion barrier. For controlling the excitation while remaining below the diffusion barrier, the pulse shape and amplitude are optimized using local optimal control theory. In particular, we use the algorithm introduced in Ref. 65, in which a variational solution for the time-local field in a dissipative system is given as a correction to a reference field $F_0(t)$ along a direction q:

$$F_q(t) = F_0(t) + \alpha(t)\text{Tr}[\hat{\mu}^{(q)}\hat{G}(t)\text{Im}[\hat{\rho}(t)]], \qquad (17)$$

where $\alpha(t) = \alpha_0[1 - \cos^{20}(\pi t/t_f)]$ enforces the proper initial and final conditions, and α_0 is a user-defined penalty factor. The operator $\hat{G}(t)$ defines a time-dependent target, which is here chosen as a sum of projectors on the states of interest weighted by Gaussians evolving in time, $w_k(t)$:

$$\hat{G}(t) = \sum_k w_k(t)|k\rangle\langle k|. \qquad (18)$$

The results of the optimization for $\alpha_0 = 5$ are shown in the central panel of Fig. 7, along with the Fourier transform of the field. The reference field $F_0(t)$ is chosen as the π pulse tailored to excite the S mode. Although the excitation yield is only marginally improved at 40%, the field selectivity is almost perfect. From the excited population, only a small portion is now found in the second excited state and almost none in the third, with the intermode population transfer completely suppressed. The excitation to state $|3,0,0,0;c\rangle$, which could serve as an intermediate to favor diffusion, is shown in the bottom panel. Due to the high intensity of the optimized field, the population of the states depicted represents only about 65% of the full system dynamics. Since all the pure S-mode states are shown in the figure, this indicates that many intermode transitions occurred. In comparison to the π pulse, the target
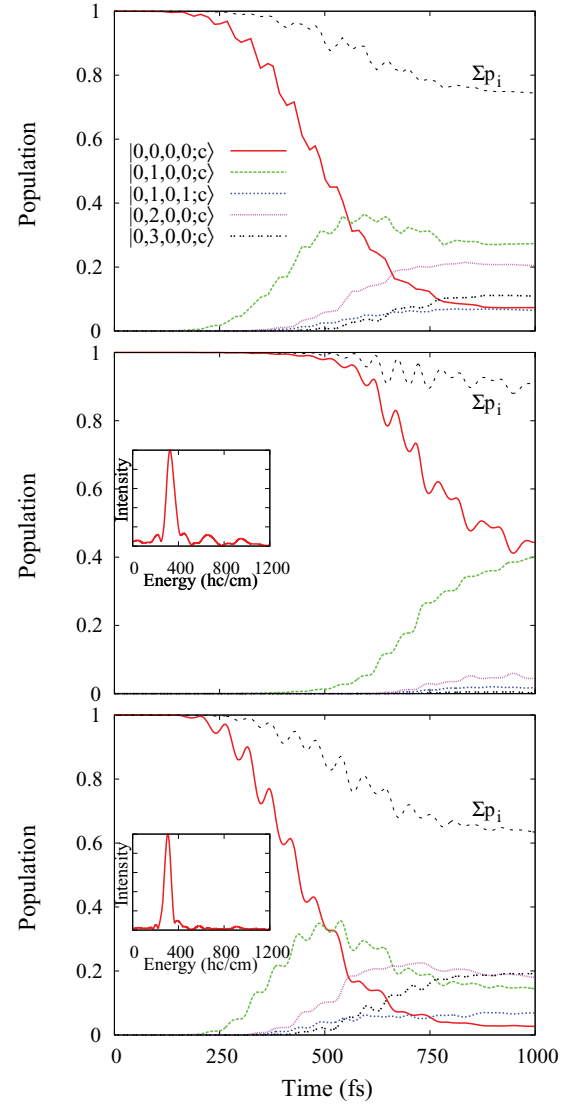

FIG. 7. (Color online) Excitation of the S mode using short z-polarized laser fields. The ground state, the first, second, and third excited states, as well as the mixed Z-ϕ state are shown in solid red, dashed green, dotted magenta, dotted black, and dotted blue, respectively. The sum of the population of the states depicted is shown as dashed gray lines ($\sum p_i$). Top panel: π pulse excitation. Central panel: Locally optimal pulse for the direct excitation of state $|0,1,0,0;c\rangle$ ($\alpha_0 = 5$, fluence: $f = 780$ mJ/cm^2). Bottom panel: Locally optimal pulse for the sequential excitation of state $|0,3,0,0;c\rangle$; $\alpha_0 = 5$. ($\alpha_0 = 5$, fluence: $f = 2.0$ J/cm^2) The Fourier transforms of the optimized fields are shown in their respective insets.

state population is doubled (10% versus $\sim 20\%$), with the main population loss coming from the ground and first excited states. The Fourier transform of the pulse reveals a single dominant peak centered at the S-mode transition frequency. A slight asymmetry toward the lower energies can be seen, which accommodates the anharmonicity along the vibrational ladder. In contrast, the pulse tailored to achieve excitation of the fundamental band contains three main components (see inset in the central panel). The two higher frequencies are centered at the S-mode overtones and prevent further excitation.
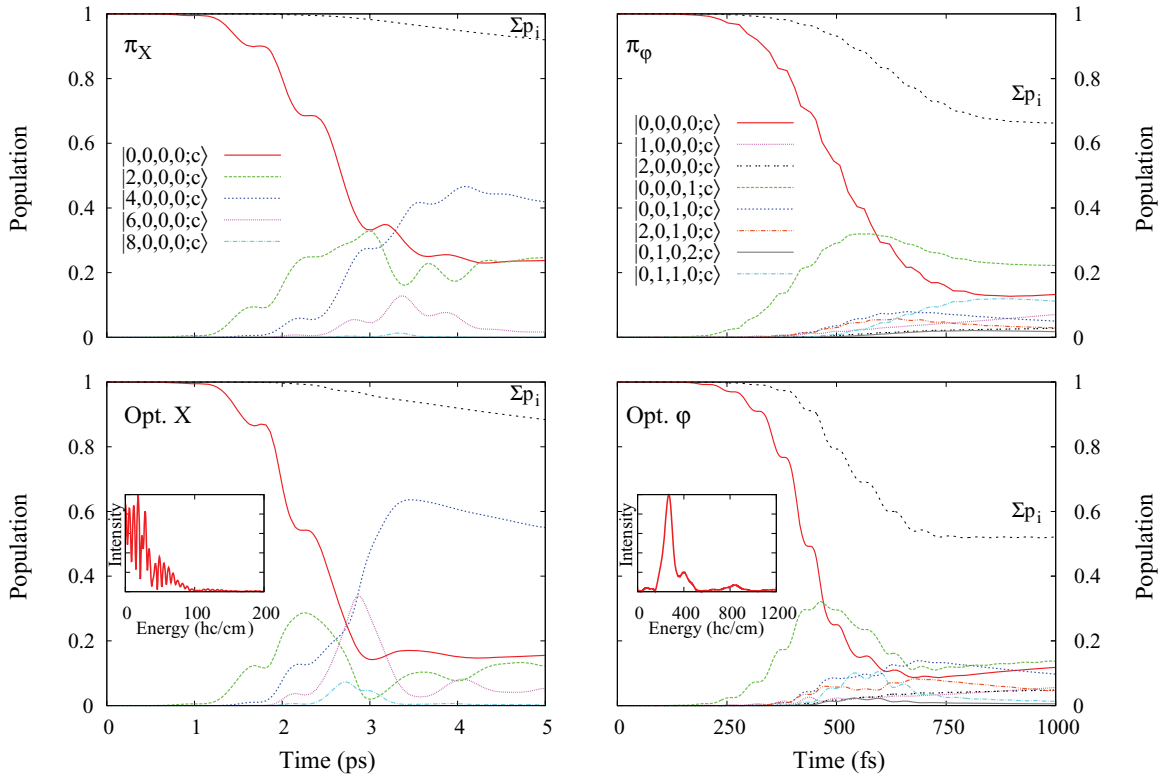
FIG. 8. (Color online) Excitation of the T mode and of the R mode using short polarized laser fields. The sum of the population of the states depicted is shown as dashed gray lines ($\sum p_i$). Top left panel: z-polarized π pulse excitation of the T mode. The ground state (solid red), as well as the second (dashed green), fourth (dotted blue), sixth (dashed magenta), and eighth (dashed dotted cyan) excited states, are shown. Bottom left panel: Locally optimal z-polarized pulse for the sequential excitation of state $|0,4,0,0;c\rangle$ ($\alpha_0 = 0.1$, fluence: $f = 56$ mJ/cm^2) and its Fourier transform (see inset). The key is the same as in the top right panel. Top right panel: x-polarized π pulse excitation of the R mode. States $|0,0,0,0;c\rangle$ (solid red), $|1,0,0,0;c\rangle$ (dashed magenta), $|2,0,0,0;c\rangle$ (dotted black), $|0,0,0,1;c\rangle$ (dashed green), $|0,0,1,0;c\rangle$ (dotted blue), $|2,0,1,0;c\rangle$ (dashed dotted orange), $|0,1,0,2;c\rangle$ (dotted gray), and $|0,1,1,0;c\rangle$ (dashed dotted cyan) are depicted. Bottom right panel: Locally optimal x-polarized pulse for the sequential excitation of state $|0,0,1,0;c\rangle$ ($\alpha_0 = 10$, fluence: $f = 3.0$ J/cm^2). The key is the same as in the top right panel. The Fourier transforms of the optimized fields are shown in their respective insets.

Figure 8 shows the population evolution for the excitation along the T mode (left panels) and the R mode (right panels) using, respectively, z and x polarized pulses. The top panels show the results for π pulses and the bottom panels show those for locally optimal control pulses. From the top left panel, it can be seen that the even overtones can be populated efficiently, as expected from the transition dipole moments. The pulse was chosen somewhat longer (5 ps) to favor the selectivity of the transition by reducing dynamical broadening. The long lifetime of the T mode (108 ps) means that dissipation should not play a dominant role in the dynamics. Since the fourth excited state has the largest yield we tailor a pulse to reach specifically this target, the result of which can be seen from the bottom left panel. As was the case for the S-mode excitation, the yield is only marginally improved from ~42% from the π pulse to ~55%, while selectivity is greatly improved. Dissipation already plays a small role in the dynamics, as can be seen from the decay after the target population reached a maximum at about 3.25 ps. According to the harmonic rule, the fourth excited state has an estimated lifetime of 27 ps, which is close to our value of 25.9 ps for the associated inverse transition rate ($|4,0,0,0;c\rangle \rightarrow |3,0,0,0;c\rangle$). On the other hand, anharmonic coupling opens a further dissipation

channel from $|4,0,0,0;c\rangle$ to $|2,0,0,0;c\rangle$ which dominates the relaxation dynamics (with an inverse transition rate of 22.9 ps). Although the estimated lifetime is in good agreement with our findings, the crude harmonic model gives a qualitatively wrong microscopic picture of the relaxation mechanism.

The situation is quite similar for the R-mode activation. Upon excitation using a 1-ps x-polarized π pulse tuned at the first transition frequency, many combination bands and other modes are populated (see top right panel of Fig. 8). These include pure T-mode states, as well as mixed T-mode, S-mode, and θ states. This is an indicator that most of the intermode coupling is mediated by the angular degrees of freedom. Further, only part of the population dynamics could be illustrated here, as many other states get populated either by the direct excitation or by subsequent relaxation. To try favoring the diffusion motion, it would be desirable to excite the θ state so as to induce a tilting motion. The optimization result is shown in the bottom right panel of Fig. 8. The field fluence becomes very large ($f = 3.0$ J/cm^2), which induces even more undesirable intermode excitation. The population increase from ~5% to ~10% is far from satisfying and is a consequence of the short lifetime of the θ state, which relaxes within 862 fs to the ground state. The remaining 50% of the
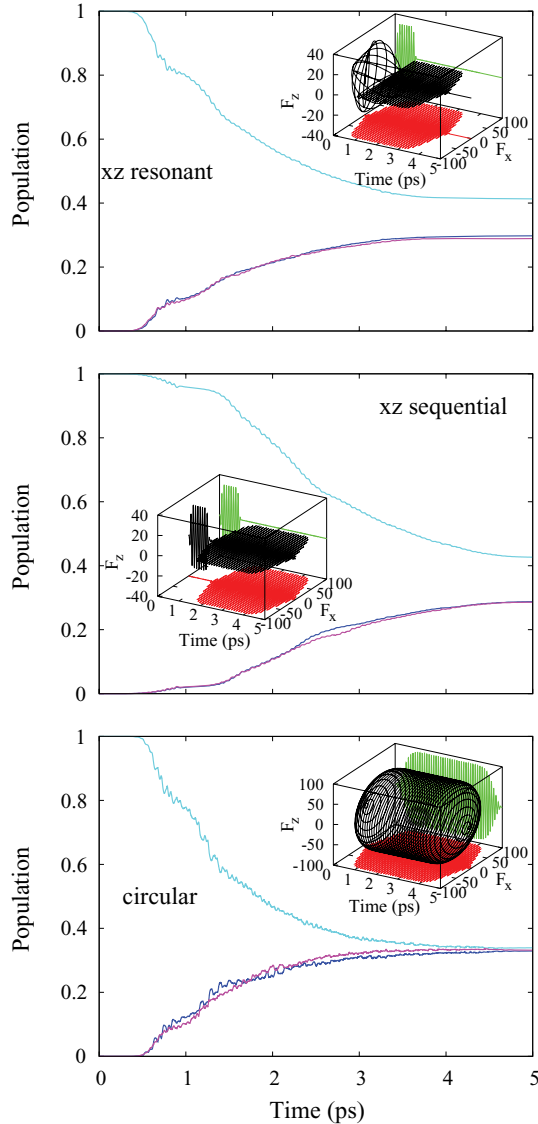
FIG. 9. (Color online) Diffusion along the x direction using xz-polarized laser fields. The sums of populations in the left, central, and right wells are depicted in cyan, blue, and magenta, respectively. Top panel: Simultaneous resonant pulses for the S-mode (z-polarized, with $\hbar\omega = 308$ hc/cm and a duration of 1 ps) and R-mode (x-polarized, with $\hbar\omega = 288$ hc/cm and a duration of 4 ps) excitations. Central panel: Sequential resonant pulses using the same parameters as above. Bottom panel: Circularly polarized pulse with energy $\hbar\omega = 308$ hc/cm and dephasing $\varphi = \pi/2$. The fields' time profiles (in MV/cm), along with their projection on the x (F_x, red) and z (F_z, green) axes, are shown in black in their respective insets.

population is still located in the central well and spread on many states.

All the above excitations were performed within a single potential energy well along the X coordinate using the localized basis described in Sec. II B. Since the vertical excitations could not favor diffusion we resort to combination of pulses polarized along the x and z directions. Figure 9 shows the time evolution of the sum of populations in the different wells for simultaneous ("xz resonant," top panel) and sequential ("xz sequential," central panel) pulses. To enhance
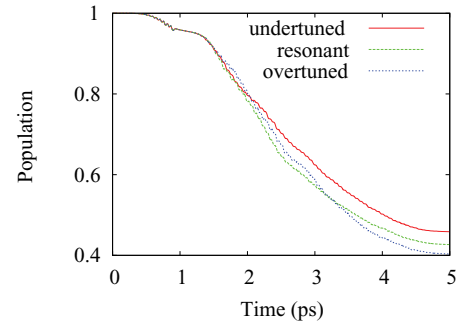

FIG. 10. (Color online) Population of the states localized on top of the central copper atom excited simultaneously by a 1-ps z-polarized pulse and a 4-ps x-polarized pulse. The z-polarized pulse is tuned to the S-mode frequency ($\hbar\omega = 308$ hc/cm). The frequency of the x-polarized pulse is chosen as $\hbar\omega_u = 269$ hc/cm ("undertuned," red), $\hbar\omega_{res} = 288$ hc/cm ("resonant," green), and $\hbar\omega_o = 310$ hc/cm ("overtuned," blue).

the bouncing motion on top of the central copper atom, a z-polarized π pulse of duration 1 ps tuned at the S-mode frequency ($\hbar\omega = 308$ hc/cm) is used. An x-polarized pulse of duration 4 ps and amplitude $F_{0,x} = 100$ MV/cm tuned at the R-mode frequency ($\hbar\omega = 288$ hc/cm) is used to enforce lateral motion and promote the lateral displacement. The resulting fields (black line), as well as their projections on the z (green) and x (red) axes, are shown in the insets. At the end of the simultaneous pulse, about the same population coming from the central well (i.e., adsorbed on top of the central copper atom) is transferred to either the left (29.8%) or right (28.9%) wells. The situation is similar for the sequential pulse, where 28.8% and 28.5% of the population are found, respectively, in the left and right wells. By taking into account the numerical errors associated with the localization procedure, the differences concerning the preferred direction of the diffusion cannot be considered significant. Still, it remains that the dephasing between the two pulses plays a small role in favoring diffusion. As can be seen by comparing the left and right well populations at around 1 ps, the major contribution to diffusion comes from excitation of the R mode using an x-polarized pulse. Only a small population transfer to the side wells (about 5%) is observed at the end of the "pure" z-polarized pulse (see central panel), whereas it appears as a shoulder on the curve obtained for the simultaneous pulses. This is partially due to the larger amplitude of the field along the x direction.

Detuning the frequency of the x-polarized pulse up to about $\pm10\%$ around the resonance energy did not influence greatly the excitation selectivity, while it affects somewhat the transfer yields. This can be taken from Fig. 10, where the population in the central well is shown for three sample frequencies. Since the field with higher frequency performs better, a simpler field containing two components tuned at the S-mode excitation energy could be used to favor diffusion. The bottom panel of Fig. 9 shows the population evolution of the three wells driven by a circularly polarized field of the form (in Cartesian representation)

$$\vec{F}(t) = F_0 U(t) \begin{pmatrix} \cos(\omega_0 t) \\ 0 \\ \cos(\omega_0 t + \varphi) \end{pmatrix}. \tag{19}$$

Here, $U(t) = 1 - \cos^{20}(\frac{\pi t}{\Delta T})$ is the pulse shape, F_0 is its amplitude, and $\hbar\omega_0 = 308\ hc/$cm is its frequency. The phase shift between the x and z components is set to $\varphi = \pi/2$. The resulting field and the associated projections are depicted in the inset. One can see that the circularly polarized pulse performs better than the sequential and simultaneous pulses proposed above. At the end of the propagation, a statistical mixture of populations in all three wells is obtained. The improved diffusion is partly due to the overtuning of the z component of the field with respect to the resonant frequency, but it is also due to the larger field amplitude along the z axis. Again, no preferred direction was found for the diffusion. It appears that directionality cannot be implemented using such simple rational pulses. Other control strategies, such as position-dependent heating and cooling cycles or coherent wave packet control, could potentially perform better but were not further investigated here.

V. CONCLUSION

In conclusion, we have investigated the excitation and relaxation dynamics of CO on Cu(100) within the reduced density matrix formalism in its Lindblad form. A model 4D Hamiltonian for studying local excitations and diffusion along the x axis was proposed. The wave functions were computed variationally using a new variant of the inexact spectral transform Lanczos method to favor convergence of the lowest lying eigenstates. A novel numerical scheme for the localization of sets of three delocalized wave functions was proposed and applied to the 4D eigenstates of the CO/Cu(100) system, yielding a physically sound basis set of localized functions to study diffusion at the surface. The relaxation rate due to electron-hole pair coupling was computed using an anharmonic perturbative rate approach. The corrugation and the intermode coupling were taken into account by including the position dependence of the nonadiabatic interactions.

From the relaxation dynamics it can be seen that intermode coupling plays an important role in the energy redistribution among the molecular vibrations at the surface. It appears that the θ angle is particularly important for mediating the energy redistribution. This is not what would be expected from the single-mode harmonic picture usually used to compute state-resolved transition rates. Further, a rigorous assignment of the quantum numbers of the different modes is necessary for the latter model, which is not possible here due to the strong anharmonic coupling of the 4D vibrational wave functions. The simplistic picture is bound to provide a false depiction of the microscopic relaxation dynamics, whereas our model proposes a more complete and balanced description.

Surprisingly, the direct relaxation of angular ϕ states to the ground state is not found to be the dominating dissipative channel, but rather the conversion to the frustrated translation mode dominates. The relaxation of the latter is strongly affected by anharmonicity to the unforeseen extent that multiple-quanta deexcitation even dominates for higher T-mode excited states. Relaxation between different wells was also observed for states well above the diffusion barrier but was not significant for strongly localized states.

The dissipative dynamics was driven by short, intense laser fields. Using a new global model dipole moment surface, we demonstrated that selective excitation of the modes perpendicular and parallel to the surface could be achieved, while state selectivity could be attained with partial success using time-local control theory. Various polarized pulses were tailored to transfer population from one adsorption site to the others along the diffusion coordinate with partial success. It was even possible to create a statistical mixture using a slightly detuned field polarized in the xz plane. Efforts to enforce directionality to the diffusion motion were in vain, most probably due to the surface symmetry. Other types of control scenarios, which will be the subject of future work, could produce better results.

*jean.c.tremblay@gmail.com

[1] N. Camillone III, K. Khan, P. J. Lasky, L. Wu, J. E. Moryl, and R. M. Osgood Jr., J. Chem. Phys. **109**, 8045 (1998).

[2] M. Bonn, S. Funk, C. Hess, D. N. Denzler, C. Stampfl, M. Scheffler, M. Wolf, and G. Ertl, Science **285**, 1042 (1999).

[3] N. Koumura, R. W. Zijlstra, R. A. van Delden, and B. L. Harada, N. Freinga, Nature (London) **401**, 152 (1999).

[4] C. Joachim, J. K. Gimzewski, and A. Aviram, Nature **408**, 541 (2000).

[5] J. C. Tully, Annu. Rev. Phys. Chem. **51**, 153 (2000).

[6] K. Watanabe, N. Takagi, and Y. Matsumoto, Chem. Phys. Lett. **366**, 606 (2002).

[7] D. Denzler, C. Frischkorn, C. Hess, M. Wolf, and G. Ertl, Phys. Rev. Lett. **91**, 226102 (2003).

[8] K. Hoki, M. Yamaki, and Y. Fujimura, Angew. Chem. Int. Ed. **115**, 3084 (2003).

[9] K. Hoki, M. Yamaki, R. Sahnoun, L. González, S. Keseci, and Y. Fujimura, J. Phys. Chem. B **108**, 4916 (2004).

[10] D. N. Denzler, C. Frischkorn, M. Wolf, and G. Ertl, J. Phys. Chem. B **108**, 14503 (2004).

[11] L. Bartels, F. Wang, D. Möller, and T. Knoesel, E. Heinz, Science **305**, 648 (2004).

[12] K. Stépan, J. Güdde, and U. Höffer, Phys. Rev. Lett. **94**, 236103 (2005).

[13] P. Saalfrank, Chem. Rev. **106**, 4116 (2006).

[14] M. Bonn, C. Hess, and M. Wolf, J. Chem. Phys. **115**, 7725 (2001).

[15] T. Vazhappilly, S. Beyvers, T. Klamroth, M. Luppi, and P. Saalfrank, Chem. Phys. **338**, 299 (2007).

[16] T. Vazhappilly, T. Klamroth, P. Saalfrank, and R. Hernandez, J. Phys. Chem. C 113, 7790 (2009).

[17] G. Füchsel, T. Klamroth, J. C. Tremblay, and P. Saalfrank, Phys. Chem. Chem. Phys. 12, 14082 (2010).

[18] G. Füchsel, T. Klamroth, S. Monturet, and P. Saalfrank, Phys. Chem. Chem. Phys. 13, 8659 (2011).

[19] J. C. Tremblay, S. Monturet, and P. Saalfrank, J. Phys. Chem. A 115, 10698 (2011).

[20] J. C. Tremblay and P. Saalfrank, J. Chem. Phys. 131, 084716 (2009).

[21] V. S. Letokhov, Science 180, 451 (1973).

[22] F. F. Crim, Science 249, 1387 (1990).

[23] M. Shapiro and P. Brumer, J. Chem. Phys. 98, 201 (1993).

[24] P. Nieto, E. Pijper, D. Barredo, G. Laurent, R. A. Olsen, E.-J. Baerends, G.-J. Kroes, and D. Farías, Science 312, 86 (2006).

[25] J. I. Juaristi, M. Alducin, R. Díez Muiño, H. F. Busnengo, and A. Salin, Phys. Rev. Lett. 100, 116102 (2008).

[26] A. C. Luntz, I. Makkonen, M. Persson, S. Holloway, D. M. Bird, and M. S. Mizielinski, Phys. Rev. Lett. 102, 109601 (2009).

[27] J. I. Juaristi, M. Alducin, R. Díez Muiño, H. F. Busnengo, and A. Salin, Phys. Rev. Lett. 102, 109602 (2009).

[28] G.-J. Kroes, C. Diaz, E. Pijpera, R. A. Olsena, and D. J. Auerbach, Publ. Natl. Acad. Sci. USA 107, 20881 (2010).

[29] M. Head-Gordon and J. C. Tully, J. Chem. Phys. 96, 3939 (1992).

[30] A. M. Wodtke, D. Matsiev, and D. J. Auerbach, Prog. Surf. Sci. 83, 167 (2008).

[31] J. C. Tully and R. K. Preston, J. Chem. Phys. 55, 562 (1971).

[32] N. A. Shenvi, S. Roy, and J. C. Tully, J. Chem. Phys. 130, 174107 (2009).

[33] S. Roy, N. A. Shenvi, and J. C. Tully, J. Chem. Phys. 130, 174716 (2009).

[34] M. S. Mizielinski and D. M. Bird, J. Chem. Phys. 132, 184704 (2010).

[35] D. Matsiev, Z. Li, R. Cooper, I. Rahinov, C. Bartels, D. J. Auerbach, and A. M. Wodtke, Phys. Chem. Chem. Phys. 13, 8153 (2011).

[36] C. Bartels, R. Cooper, D. J. Auerbach, and A. M. Wodtke, Chem. Sci. 2, 1647 (2011).

[37] B. Hellsing and M. Persson, Phys. Scr. 29, 360 (1984).

[38] B. N. J. Persson, J. Phys. C 17, 4741 (1984).

[39] V. Krishna and J. C. Tully, J. Chem. Phys. 125, 054706 (2006).

[40] M. Timmer and P. Kratzer, Phys. Rev. B 79, 165407 (2009).

[41] M. Richter, A. Carmele, S. Butscher, N. Bücking, F. Milde, P. Kratzer, M. Scheffler, and A. Knorr, J. Appl. Phys. 105, 122409 (2009).

[42] M. J. Puska and R. M. Nieminen, Phys. Rev. B 27, 6121 (1983).

[43] H. Winter, J. I. Juaristi, I. Nagy, A. Arnau, and P. M. Echenique, Phys. Rev. B 67, 245401 (2003).

[44] J. C. Tremblay, S. Monturet, and P. Saalfrank, Phys. Rev. B 81, 125408 (2010).

[45] G. Füchsel, J. C. Tremblay, T. Klamroth, and P. Saalfrank, Isr. J. Chem. 52, 438 (2012).

[46] S. Carter, S. J. Culik, and J. M. Bowman, J. Chem. Phys. 107, 10458 (1997).

[47] A. Bahel and Z. Bačić, J. Chem. Phys. 111, 11164 (1999).

[48] J. Blomquist and O. Uvdal, Phys. Chem. Chem. Phys. 12, 14162 (2010).

[49] M. Ceotto, D. Dell'Angelo, and G. F. Tantardini, J. Chem. Phys. 133, 054701 (2010).

[50] C. Cattarius and H.-D. Meyer, J. Chem. Phys. 121, 9283 (2004).

[51] A. S. Leathers, D. A. Micha, and D. S. Kilin, J. Chem. Phys. 131, 144106 (2009).

[52] S. Beyvers, Y. Ohtsuki, and P. Saalfrank, J. Chem. Phys. 124, 234706 (2006).

[53] J. C. Tremblay, S. Beyvers, and P. Saalfrank, J. Chem. Phys. 128, 194709 (2008).

[54] J. C. Tully, M. Gomez, and M. Head-Gordon, J. Vac. Sci. Technol. A 11, 1914 (1993).

[55] R. Marquardt, F. Cuvelier, R. A. Olsen, E. J. Baerends, J. C. Tremblay, and P. Saalfrank, J. Chem. Phys. 132, 074108 (2010).

[56] G. K. Paramonov, I. Andrianov, and P. Saalfrank, J. Phys. Chem. C 111, 5432 (2007).

[57] R. Kosloff, S. A. Rice, P. Gaspard, S. Tersigni, and D. J. Tannor, Chem. Phys. 139, 201 (1989).

[58] R. Kosloff, A. D. Hammerich, and D. J. Tannor, Phys. Rev. Lett. 69, 2172 (1992).

[59] M. Sugawara and Y. Fujimara, J. Chem. Phys. 100, 5646 (1994).

[60] D. J. Tannor, in Molecule in Laser fields, edited by A. J. Bandrauk (Dekker, New York, 1992), p. 413.

[61] Y. Ohtsuki, H. Kono, and Y. Fujimura, J. Chem. Phys. 109, 9318 (1998).

[62] Y. Ohtsuki, Y. Yahata, H. Kono, and Y. Fujimura, Chem. Phys. Lett. 287, 627 (1998).

[63] Y. Zhao and O. Kühn, J. Phys. Chem. A 104, 4882 (2000).

[64] F. L. Yip, D. A. Mazziotti, and H. Rabitz, J. Phys. Chem. A 107, 7264 (2003).

[65] J. C. Tremblay and P. Saalfrank, Phys. Rev. A 78, 063408 (2008).

[66] J. C. Tremblay, J. Chem. Phys. 134, 174111 (2011).

[67] R. N. Zare, Angular Momentum (Wiley, New York, 1988).

[68] J. C. Light, I. P. Hamilton, and J. V. Lill, J. Chem. Phys. 82, 1400 (1985).

[69] J. T. Muckerman, Chem. Phys. Lett. 173, 200 (1990).

[70] C. Leforestier, J. Chem. Phys. 94, 6388 (1991).

[71] D. T. Colbert and W. H. Miller, J. Chem. Phys. 96, 1982 (1992).

[72] J. Echave and D. C. Clary, Chem. Phys. Lett. 190, 225 (1992).

[73] H. Wei and T. Carrington Jr., J. Chem. Phys. 97, 3029 (1992).

[74] M. J. Bramley and T. Carrington Jr., J. Chem. Phys. 99, 8519 (1993).

[75] H. Wei, J. Chem. Phys. 106, 6885 (1997).

[76] J. C. Light and T. Carrington Jr., Adv. Chem. Phys. 114, 263 (2000).

[77] H.-G. Yu, J. Chem. Phys. 122, 164107 (2005).

[78] J. C. Tremblay and T. Carrington Jr., J. Chem. Phys. 125, 094311 (2006).

[79] H.-G. Yu and S. C. Smith, Ber. Bunsen-Ges. Phys. Chem. 101, 400 (1997).

[80] H.-G. Yu and G. Nyman, J. Chem. Phys. 110, 11133 (1999).

[81] S.-W. Huang and T. Carrington Jr., J. Chem. Phys. 112, 8765 (2000).

[82] S.-W. Huang and T. Carrington Jr., J. Chem. Phys. 114, 6485 (2001).

[83] S.-W. Huang and T. Carrington Jr., Appl. Numer. Math. 37, 307 (2001).

[84] C. J. Hirschmugl, G. P. Williams, F. M. Hofmann, and Y. J. Chabal, Phys. Rev. Lett. 65, 480 (1990).

[85] F. Hofmann and J. P. Toennies, Chem. Rev. 96, 1307 (1996).

[86] A. P. Graham, F. Hofmann, J. P. Toennies, G. P. Williams, C. J. Hirschmugl, and J. Ellis, J. Chem. Phys. 108, 7825 (1998).

[87] G. Lindblad, Commun. Math. Phys. 48, 119 (1976).

[88] J. C. Tremblay and T. Carrington Jr., J. Chem. Phys. 121, 11535 (2004).

[89]J. C. Tremblay, T. Klamroth, and P. Saalfrank, J. Chem. Phys. **129**, 084302 (2008).

[90]J. P. Perdew and Y. Wang, Phys. Rev. B **45**, 13244 (1992).

[91]G. Kresse and J. Furthmuller, Phys. Rev. B **54**, 11169 (1996).

[92]G. Kresse and J. Furthmuller, Comput. Math. Sci. **6**, 15 (1996).

[93]H. J. Monkhorst and J. D. Pack, Phys. Rev. B **13**, 5188 (1976).

[94]T. Yanai, D. Tew, and N. Handy, Chem. Phys. Lett. **393**, 51 (2004).

[95]M. J. Frisch *et al*., GAUSSIAN09 *Revision A.02*, Gaussian Inc. Wallingford, CT, 2009.

[96]P. J. Hay and W. R. Wadt, J. Chem. Phys. **82**, 270 (1985).

[97]W. R. Wadt and P. J. Hay, J. Chem. Phys. **82**, 284 (1985).

[98]P. J. Hay and W. R. Wadt, J. Chem. Phys. **82**, 299 (1985).

[99]A. K. Wilson, T. van Mourik, and T. H. Dunning, J. Mol. Struct. **388**, 339 (1996).

[100]J. M. Ricart, A. Clotet, F. Illas, and J. Rubio, J. Chem. Phys. **100**, 1988 (1994).